UC San Diego
UC San Diego Previously Published Works

Title

Carbon-free high-loading silicon anodes enabled by sulfide solid electrolytes.

Permalink

https://escholarship.org/uc/item/2vt9r39s

Journal

Science (New York, N.Y.), 373(6562)

ISSN

0036-8075

Authors

Tan, Darren HS
Chen, Yu-Ting
Yang, Hedi
et al.

Publication Date

2021-09-01

DOI

10.1126/science.abg7217

Peer reviewed

Carbon-free high-loading silicon anodes enabled by sulfide solid electrolytes

Darren H. S. Tan[1], Yu-Ting Chen[1], Hedi Yang[1], Wurigumula Bao[1], Bhagath Sreenarayanan[1], Jean-Marie Doux[1], Weikang Li[1], Bingyu Lu[1], So-Yeon Ham[1], Baharak Sayahpour[1], Jonathan Scharf[1], Erik A. Wu[1], Grayson Deysher[1], Hyea Eun Han[2], Hoe Jin Hah[2], Hyeri Jeong[2], Jeong Beom Lee[2], Zheng Chen[1,3,4,5]*, Ying Shirley Meng[1,4,5]*

The development of silicon anodes for lithium-ion batteries has been largely impeded by poor interfacial stability against liquid electrolytes. Here, we enabled the stable operation of a 99.9 weight % microsilicon anode by using the interface passivating properties of sulfide solid electrolytes. Bulk and surface characterization, and quantification of interfacial components, showed that such an approach eliminates continuous interfacial growth and irreversible lithium losses. Microsilicon full cells were assembled and found to achieve high areal current density, wide operating temperature range, and high areal loadings for the different cells. The promising performance can be attributed to both the desirable interfacial property between microsilicon and sulfide electrolytes and the distinctive chemomechanical behavior of the lithium-silicon alloy.

S ilicon (Si), which has a specific capacity exceeding 3500 mAh g^{-1}, has emerged as a promising alternative to graphite-based anodes (with a specific capacity of ~370 mAh g^{-1}) to increase the energy densities of lithium-ion batteries (LIBs), for various energy-storage applications such as electric vehicles and portable devices (*1, 2*). In addition to being the second most abundant element in Earth's crust, Si is also environmentally benign and exhibits electrochemical potentials close to that of graphite (0.3 V versus Li/Li$^+$) (*2*). However, commercialization of Si anodes is hindered by its poor cycling and shelf life resulting from continuous solid electrolyte interphase (SEI) growth between the highly reactive Li-Si alloy and organic liquid electrolytes used in LIBs. These deficiencies are exacerbated by the large volumetric expansion (>300%) of Si during lithiation and by the loss of Li$^+$ inventory due to SEI growth and irreversibly trapped Li-Si alloy enclosed within (*3*).

Current efforts to mitigate capacity fade include the use of sophisticated Si nanostructures in combination with carbon composites and robust binder matrix to mitigate pulverization (*1, 3–6*). Liquid electrolyte modifications, including the use of cyclic ethers, fluorinated additives, or other ionic liquids additives that stabilize the SEI, have also been explored (*5, 7*). Improvements have been reported in numerous half-cell studies, but the varied amounts of lithium excess make it challenging to evaluate the effectiveness of each strategy. Among reports that demonstrated stable cycling in full cells (*5, 8–20*), most are limited to 100 cycles, apart from a few that demonstrated longer cycle life using various prelithiation strategies to compensate for Li$^+$ inventory losses (*9, 14, 18*). Although prelithiation can be effective to extend cycle life, the ideal Si anode should be composed of pristine microsilicon (μSi) particles that do not require further treatment, reaping the benefits of low costs, ambient air stability, and environmentally benign properties. To realize this potential, two key challenges should be addressed: (i) stabilizing the Li-Si | electrolyte interface to prevent continuous SEI growth and trapped Li-Si accumulation, and (ii) mitigating growth of new interfaces induced by volume expansion that results in Li$^+$ consumption.

Si stability problems arise mainly from the interface with liquid electrolytes. The use of solid-state electrolytes (SSEs) in an all solid-state battery (ASSB) is a promising alternative approach, owing to its ability to form a stable and passivating SEI (*21*). Previous studies have reported the use of thin (submicrometer)–film type Si in ASSBs (*11, 22, 23*). Most ASSB reports have focused on the use of metallic Li, in an effort to maximize cell energy densities (*24, 25*). However, small critical current densities of metallic Li anodes often dictate the need for operation under elevated temperatures, especially during cell charging. In this work, a μSi electrode consisting of 99.9 wt % μSi is used in μSi||SSE||lithium nickel cobalt manganese oxide (NCM811) cells to overcome both the interfacial stability challenges of μSi and the current density limitations of ASSBs.

Unlike conventional liquid-cell architectures, the SSE does not permeate through the porous μSi electrode (Fig. 1), and the interfacial contact area between the SSE and the μSi electrode is reduced to a two-dimensional (2D) plane. After lithiation of μSi, the 2D plane is retained despite volume expansion, preventing the generation of new interfaces. Bulk μSi exhibits an electronic conductivity of ~3 × 10^{-5} S cm^{-1} (fig. S1), comparable to that of most common cathode materials (~10^{-6} to

[1]Department of NanoEngineering, University of California San Diego, La Jolla, CA 92093, USA. [2]LG Energy Solution, Ltd., LG Science Park, Magokjungang 10-ro, Gangseo-gu, Seoul 07796, Korea. [3]Program of Chemical Engineering, University of California San Diego, La Jolla, CA 92093, USA. [4]Sustainable Power and Energy Center (SPEC), University of California San Diego, La Jolla, CA 92093, USA. [5]Program of Materials Science and Engineering, University of California San Diego, La Jolla, CA 92093, USA.
*Corresponding author. Email: shmeng@ucsd.edu (Y.S.M.); zhengchen@eng.ucsd.edu (Z.C.)
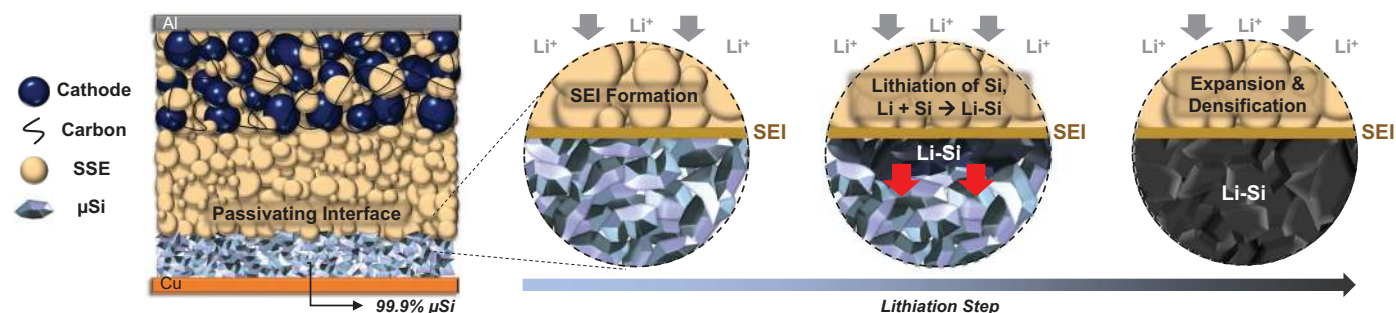
Fig. 1. Schematic of 99.9 wt % μSi electrode in an ASSB full cell. During lithiation, a passivating SEI is formed between the μSi and the SSE, followed by lithiation of μSi particles near the interface. The highly reactive Li-Si then reacts with Si particles within its vicinity. The reaction propagates throughout the electrode, forming a densified Li-Si layer.

10^{-4} S cm^{-1}) (26–28), so additional carbon additives are not necessary. Moreover, carbon is well known to be detrimental to the stability of sulfide SSEs, as it promotes SSE decomposition (29, 30). Although certain types of carbon have been found to be compatible with anode-free ASSBs (24, 31), eliminating carbon entirely in the μSi ASSB system is preferable. During lithiation of μSi, Li-Si formation can propagate throughout the electrode, benefiting from the direct ionic and electronic contact between Li-Si and μSi particles (Fig. 1). This process was found to be highly reversible without the need for any lithium excess. Separate full-cell experiments were performed, achieving current densities up to 5 mA cm^{-2}, operation between −20° and 80°C, and areal capacities of up to 11 mAh cm^{-2} (2890 mAh g^{-1}) for the different cells. Subsequent cycling of the μSi-NCM811 full cell at 5 mA cm^{-2} was found to deliver a capacity retention of 80%

after 500 cycles, demonstrating the overall robustness of μSi enabled by ASSBs.

Results

Interface characterization

To demonstrate the importance of eliminating carbon in the anode, as well as the passivating nature of the Si-SSE interface, we characterized and quantified the SEI products from SSE decomposition with and without the presence of carbon additives. As most literature reports adopt Si composites containing between 20 and 40 wt % carbon additives (5, 8–20), this was used as a basis for comparison against carbon-free μSi. Although Li metal is typically used as the counterelectrode in liquid electrolyte studies, its low critical current density in ASSBs make it unsuitable for studying our system (32, 33). Likewise, limited kinetics in lithium indium alloys also make them inappropriate (fig. S2). Thus, NCM811, which is protected

by a boron-based coating (34), was instead chosen as the counterelectrode, allowing direct evaluation of μSi in a full cell configuration without lithium excess. To prepare the samples, we used two composite Si-SSE anodes (with and without 20 wt % carbon additives). Composite anodes with SSEs were used to exaggerate any interfacial reactions for characterization. Figure 2A shows the voltage profiles of both cells during the first lithiation. The cell without carbon shows an initial voltage plateau around 3.5 V, typical of a μSi||NCM811 full cell. However, the cell with 20 wt % carbon shows a stark difference, with a lower initial plateau at 2.5 V, indicating extensive SSE electrochemical decomposition before reaching the lithiation potential above 3.5 V. Figure 2B compares the diffraction patterns of the pristine Si-SSE, lithiated Si-SSE, and lithiated Si-SSE-carbon composites. The lithiated Si-SSE sample retained the crystalline
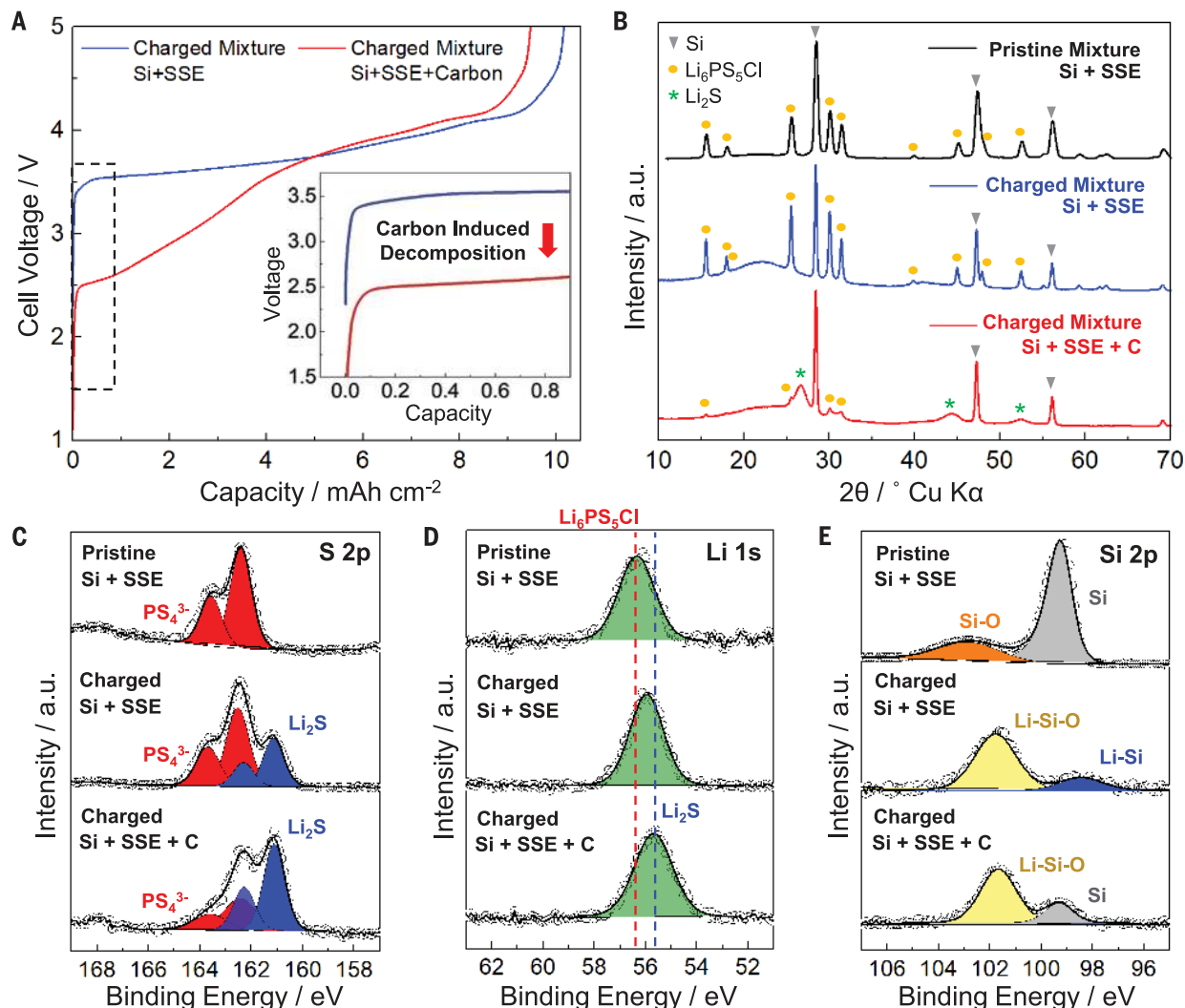

Fig. 2. Carbon effects on SSE decomposition. (**A**) Voltage profiles of μSi || SSE || NCM811 cells with and without carbon additives (20 wt %). Inset shows a lower initial plateau indicating SSE decomposition. (**B**) XRD patterns, and (**C** to **E**) XPS spectra of the (C) S 2p, (D) Li 1s, and (E) Si 2p core regions.
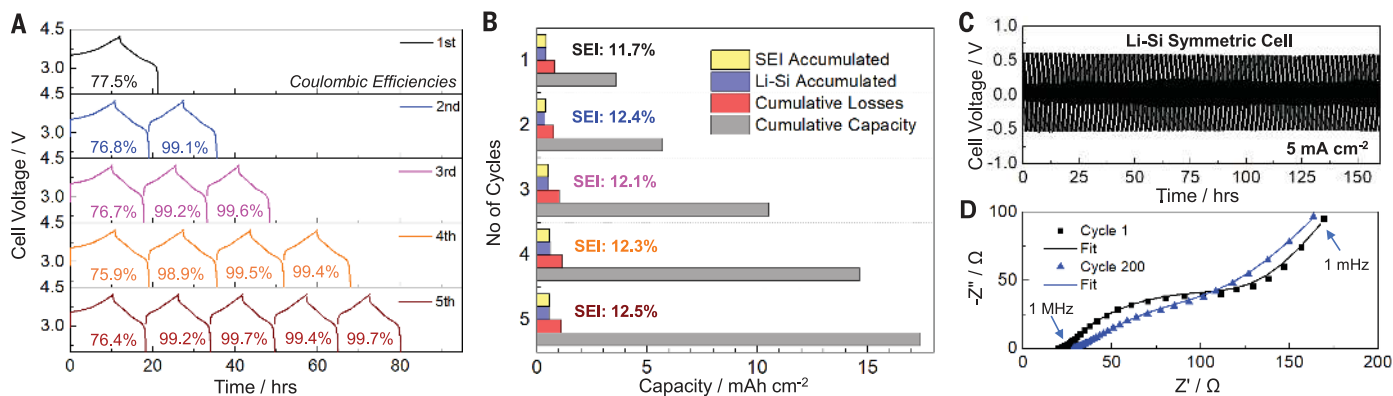
Fig. 3. Quantifying effects of SEI growth. (**A**) Voltage profiles of full cells used in titration gas chromatography. (**B**) Li-Si and SEI amounts relative to cell capacity. (**C**) Voltage profile of a Li-Si symmetric cell used for EIS, and (**D**) Nyquist plots.

structure of the SSE as well as that of the unreacted Si, with some signals of amorphous Li-Si manifesting as a hump at around 20°. Although some SEI is expected, the low amount formed at the interface is most likely not detectable with this bulk technique. However, in the cell where carbon is used, most of the pristine SSE's diffraction signals are no longer present, indicating severe electrolyte decomposition. During this process, nanocrystalline Li_2S forms as a major decomposition product and is observed as broad peaks appearing at 2θ angles of around 26°, 45°, and 52°.

These observations agree with the x-ray photoelectron spectroscopy (XPS) analysis in Fig. 2C, where the presence of carbon results in a greater extent of SSE decomposition, as seen by the formation of Li_2S (161 eV) in the S 2p region. Consequently, a larger decrease in peak intensities for the PS_4^{3-} thiophosphate unit signals is observed for the electrode containing carbon (Fig. 2C, bottom) compared to the electrode without carbon (Fig. 2C middle). Although the Li 1s region (Fig. 2D) is difficult to deconvolute owing to the presence of multiple Li^+ species, a shift toward lower binding energies is observed as a result of reduction of Li^+ from the pristine SSE. Although a smaller shift is observed in the sample without carbon (Fig. 2D middle), the peak position for the sample containing carbon is dominated by the Li_2S signals at about 55.6 eV (Fig. 2D bottom), reaffirming the previous observation using x-ray diffraction (XRD). In the Si 2p region, a native oxide layer is detected near the surface of the Si particles (Fig. 2E, top). Upon lithiation, this signal shifts to a lower binding energy. A peak with a binding energy consistent with that of Li-Si is found in the sample without carbon, whereas Si appears to remain unreacted in the sample with carbon. This is likely due to formation of the Li^+ consuming SEI products, severely limiting the lithiation of the μSi electrode itself. The vast disparities in the extent of SEI formation highlight the crit-

ical role of carbon in promoting decomposition as a result of its high specific area and electronic conductivity compared with Si. Previous studies also showed that the extent of SSE decomposition was highly dependent on the type of carbon material used, with the least decomposition observed when no carbon was used (*31*). For reduction to occur between solid-solid interfaces, sufficient contact with electronically conductive surfaces is needed. As such, carbon-free electrodes would substantially reduce SSE decomposition, resulting in improved first-cycle Coulombic efficiency (CE%) and rate capability compared with conventional carbon-containing electrodes (fig. S3, A and B).

Quantification of SEI components

Li_6PS_5Cl is reduced to form Li_2S, Li_3P, and LiCl (*29*), products that are highly passivating in nature (table S1). As such, SEI formation is expected to stabilize after the first cycle. Although capacity losses during cycling can be detected as a function of CE%, it is difficult to accurately deconvolute contributions from the SEI or trapped Li-Si, respectively. Titration gas chromatography (TGC) has been effectively used to quantify SEI and dead Li growth in Li metal batteries (*35*). In this study, TGC is similarly applied to quantify SEI growth and ascertain its passivating and stable nature. Five μSi||SSE||NCM811 full cells were assembled and cycled from one to five cycles, respectively (Fig. 3A). First-cycle CE% of ~76% was measured across all cells, which quickly rose to >99% from the second cycle. After cycling, the TGC method detailed in fig. S4 was applied to all five cells, where the difference between CE% losses and active Li^+ allows derivation of the SEI formed. The amounts of SEI accumulated, active Li^+ from Li-Si, sum of cumulative losses, and total cumulative capacities are plotted in Fig. 3B and summarized with error values in table S2. After the first cycle, the total amount of SEI formed was found to be 11.7% of the cell's capacity, and this amount

increased slightly to 12.4% in the second cycle. In the subsequent cycles, both the accumulated SEI and the active Li^+ were found to remain stable and relatively unchanged, indicating interface passivation that prevents unwanted continuous reaction between Li-Si and the electrolyte. To evaluate the SEI stability over extended cycling, we fabricated and cycled a Li-Si symmetric cell at 5 mA cm^{-2} using a capacity of 2 mAh cm^{-2} per cycle (Fig. 3C). Electrochemical impedance spectroscopy (EIS) measurements found that the impedance remained stable over 200 cycles (Fig. 3D), confirming that the SEI is passivating in nature. Enlarged voltage profiles are shown in fig. S5. Conversely, impedance growth was observed in the NCM811 symmetric cell under similar conditions (fig. S5). Table S3 details the equivalent circuits' fitted values. The stable SEI formed at the Li-Si||SSE interface may also address self-discharge challenges faced by Si anodes, especially under increased temperature where unwanted parasitic reactions are aggravated. To illustrate this, we assembled and cycled solid and liquid electrolyte-based cells for five cycles at room temperature and at 55°C (fig. S6). Compared to the liquid cell, the solid cell was able to retain its charge (~99%), even at 55°C. Subsequent self-discharge tests, with 0 to 3 days of rest time at the charged state, also showed reduced loss of charge (3% versus 28%) in the solid cell, with limited voltage decay during resting (fig. S7).

Morphological evolution

As illustrated in Fig. 1, the μSi particles in the SSE cell remain in direct ionic (Li^+) and electronic (e^-) contact with each other. This allows for fast diffusion of Li^+ and transport of e^- throughout the electrode, unhindered by any electronically insulative components such as SEI or electrolyte. Galvanostatic intermittent titration technique experiments were performed, and average Li^+ diffusion coefficients

in the range of ~10^{-9} cm^2 s^{-1} were obtained (fig. S8). These are one to two orders higher than values reported on nano-Si or Si thin films in conventional liquid electrolytes (*36–38*), which have been limited by the interfacial stability challenges and extra impedance caused by thick SEI. To visualize the morphological evolution of Li-Si, we prepared cross-section scanning electron microscopy (SEM) images of three separate μSi electrodes by focused ion beam at the pristine, lithiated, and de-lithiated states.

At the pristine state (Fig. 4A), discreet μSi particles (2 to 5 μm) were observed, with an electrode porosity of 40% after calendering. After lithiation (Fig. 4B), the electrode becomes densified, with most pores disappearing between the pristine μSi particles. Moreover, the boundaries between separate μSi particles have entirely vanished. An enlarged view of the more porous region shows that the entire electrode has become an interconnected densified Li-Si alloy. After delithiation (Fig. 4C), the μSi electrode did not revert to its original discreet microparticle structure but instead formed large particles with voids between them. It is noted that a lower loading was used to image the entire void's depth at the delithiated state. Energy-dispersive x-ray (EDS) imaging confirms that the pores are indeed voids, with no evidence of SEI or SSE present between each delithiated particle. The morphological behavior observed is in stark contrast to morphological changes of μSi particles in liquid electrolyte systems (fig. S9, A and B), where lithiated μSi particles do not merge and remain separate as a result of SEI formed throughout the electrode. This chemomechanical behavior of the Li-Si alloy has been previously reported in studies on porous Si thin-film ASSBs using sulfide SSEs as well, where initial porosity incorporated into the pristine Si thin-film electrode was found to decrease during lithiation (*11, 23*).

To quantify thickness growth and porosity changes during cycling, we prepared μSi electrodes with similar mass loadings of ~3.8 mg cm^{-2} and measured their thicknesses during charge and discharge states. At the pristine state, a thickness of ~27 μm was measured (fig. S10A), and after lithiation to Li$_{3.35}$Si, the thickness increased to ~55 μm (fig. S10B). This increase falls short of the expected >300% growth (*1*), indicating that a substantial decrease in initial 40% porosity must occur. To rationalize this, we calculated expected thicknesses versus porosities in table S4, which shows a low resulting porosity (<10%) of the ~55-μm μSi electrode after lithiation. This agrees with the qualitative observations made in Fig. 4, where considerable densification is observed compared to the pristine state. After delithiation (fig. S10C), a thickness of ~40 μm was measured, with a porosity of
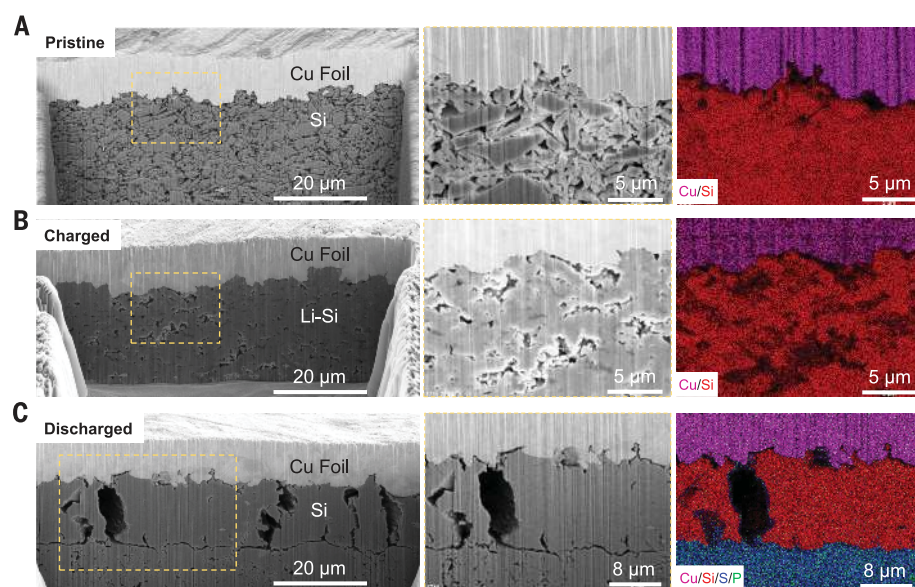

Fig. 4. Visualizing lithiation and delithiation of 99.9 wt % Si. (**A**) Pristine porous microstructure of μSi electrode. (**B**) Charged state with densified interconnected Li-Si structure. (**C**) Discharged state with void formation between large dense Si particles. Yellow dotted box represents enlarged porous regions of interest for each sample.

~30% calculated. The lower porosity at the delithiated state compared to the pristine 40% is expected, as some Li$^+$ remains in the anode (Fig. 3B). Despite the relatively large thickness and porosity changes, similar morphologies and thicknesses were observed after multiple cycles (fig. S11). This suggests that the mechanical properties of the Li-Si and SSE have a crucial role in maintaining the integrity of the interfaces as well as retaining contact with the anode along the 2D interfacial plane.

Although contact losses are less likely during lithiation, where volume expansion occurs, it is an important consideration during delithiation. However, good contact is still maintained between the SSE layer and the porous structure of the delithiated Li-Si (Fig. 4C). This indicates that some degree of Li-Si deformation occurred during cell cycling under a uniaxial applied stack pressure of 50 MPa with a homemade pressure rig (*39*). Although pristine μSi did not deform under calendering pressures of 370 MPa, existing reports found that hardness of Li-Si alloys decreases substantially as a function of lithiation, with values reaching as high as 10.0 to 11.6 GPa for pristine Si (*40, 41*), to as low as 1.3 to 1.5 GPa for fully lithiated Li$_{3.75}$Si (*40, 42*). This trend agrees with our previous observations, where lithiated Li-Si with lower hardness could undergo sufficient deformation to form a dense alloy with low porosity (Fig. 4B), whereas delithiated Li-Si with higher hardness could not be fully deformed, evident from the large interparticle voids observed (Fig. 4C). Although the stack pressure of 50 MPa applied in this study is lower than the range of Li-Si hardness values

reported in the literature, absolute conclusions on its deformability cannot be drawn from the hardness values alone. As an example, sulfide glasses, such as Li$_2$S-P$_2$S$_5$, were previously found to exhibit a hardness value of 1.9 GPa, yet they can be readily deformed at compaction pressures of 360 MPa (*43*). Likewise, crystalline Li$_6$PS$_5$Cl, which is expected to exhibit higher hardness than glassy Li$_2$S-P$_2$S$_5$, can also be deformed into a pellet for cell cycling at 50 MPa (*44*). Additionally, most mechanical studies conducted on Li-Si alloys have so far been limited to nano-indentation–based experiments on Si thin films, which can exhibit appreciably different mechanical properties compared with the μSi used in this work. As such, it is plausible for the lithiated μSi to undergo some degree of plastic deformation, especially at higher states of lithiation. To verify this, we lithiated a 99.9 wt % μSi electrode up to 0.01 V versus Li/Li$^+$ without pressure in a liquid electrolyte–based coin cell. Subsequently, we imaged the Li-Si electrode before and after pressing at 50 MPa. We observed that some degree of deformation in the lithiated Li-Si alloy was induced, along with a reduction in electrode porosity (fig. S9C). This deformation is necessary to maintain a good contact with the SSE, enabling high reversibility.

Electrochemical performance

To test the 99.9 wt % μSi in full cells, we prepared NCM811 cathode composites using a dry electrode process (fig. S12), with polytetrafluoroethylene (PTFE) as a binder to achieve thick electrodes. These electrodes were characterized by x-ray computed tomography (fig.
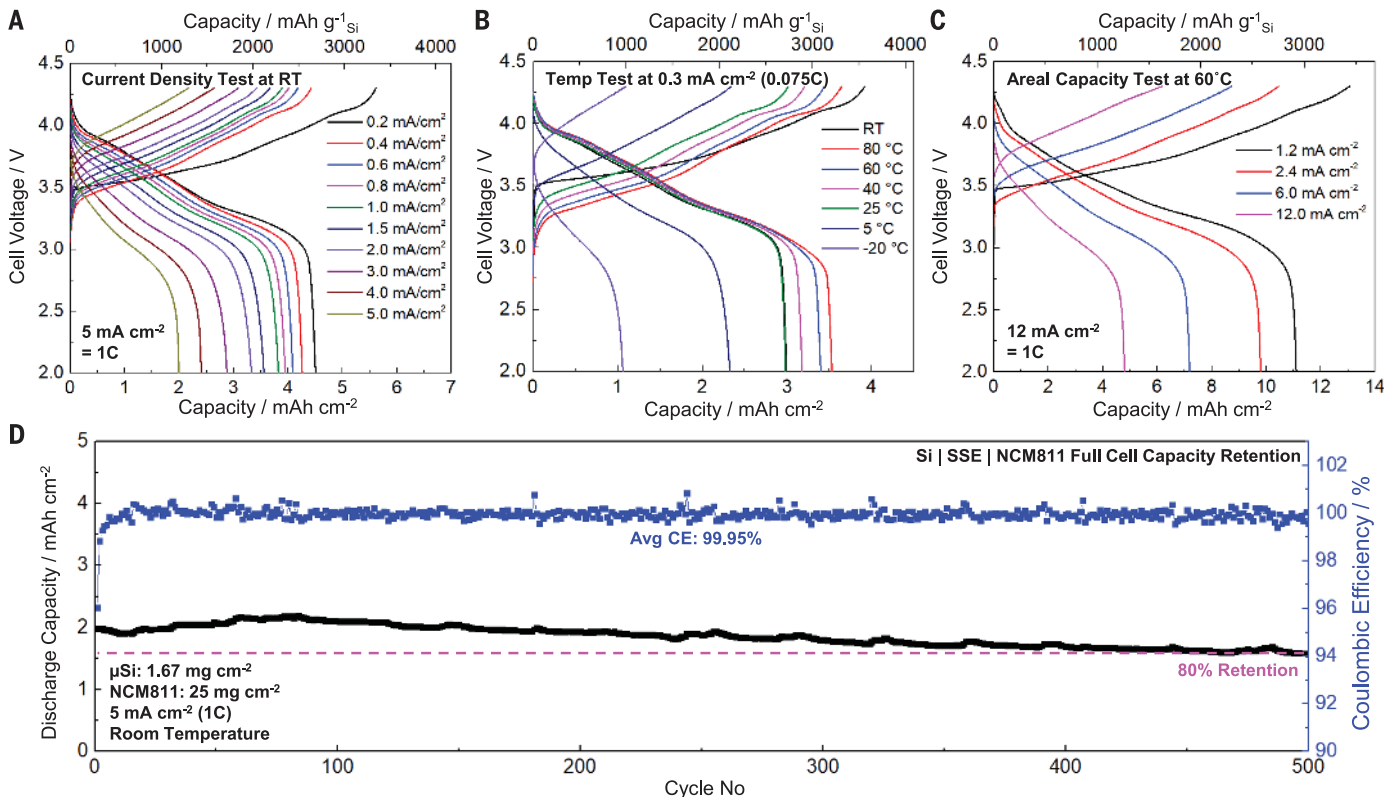
Fig. 5. μSi||SSE||NCM811 performance. (**A**) High current density test. (**B**) Wide temperature range test. (**C**) High areal capacity test. (**D**) Cycle life at room temperature. All cells were tested under similar charge and discharge conditions between 2.0 and 4.3 V. The first cycle voltage profile of each respective cell is plotted in black.

S13) and found to achieve improved electrode homogeneity and higher packing density compared with slurry casted electrodes. The dry processed cathode composites were then paired against the μSi anodes with an N/P ratio of 1.1 in full cells. Although higher N/P ratios reduce the likelihood of Li plating and cell shorting, they were found to deliver lower average CE% (fig. S14), likely as a result of higher states of charge reached by the NCM811 cathode for the same voltage cutoff, inducing undesirable impedance growth and contact losses.

Figure 5A shows the room-temperature galvanostatic cycling, where current is gradually increased from 0.2 mA cm^{-2} at the 1st cycle to 5 mA cm^{-2} at the 10th cycle. No evidence of a cell shorting occurs up to 5 mA cm^{-2} at room temperature, which is substantially higher than the typical room-temperature critical current density of Li metal ASSBs (*32, 33*). In Fig. 5B, another full cell was cycled with a temperature range between −20° and 80°C using a moderate current density of 0.3 mA cm^{-2}. A lower current density is used to overcome the high bulk impedance of the SSE at low temperatures (*45*). Nonetheless, the cell does not exhibit shorting behavior despite charging at −20°C. To evaluate high areal loadings of μSi, we fabricated a full cell with a cathode sized to 12 mAh cm^{-2} (fig. S15). To

overcome bulk impedance of the thick cathode electrode, we operated the full cell at 60°C to enhance Li^{+} diffusion kinetics (fig. S16), a temperature commonly used in ASSB reports (*24*). By cycling at 1.2 mA cm^{-2}, the μSi anode was found to deliver reversible capacities of more than 11 mAh cm^{-2} (>2890 mAh g^{-1}) (Fig. 5C). Under continuous cycling at 12 mA cm^{-2}, the μSi anode delivers stable reversible capacity of more than 5 mAh cm^{-2} (>1250 mAh g^{-1}) (fig. S12). As room-temperature charge and discharge remains the ideal condition for ASSB operation, cycle life of the full cell was evaluated by maintaining a current density of 5 mA cm^{-2} at room temperature (Fig. 5D). The cell was found to achieve a capacity retention of 80% after 500 cycles and an average CE% of >99.9%. This capacity fade likely occurs as a result of cathode-SSE contact losses and cathode impedance growth (fig. S5). As the cell's capacity utilization at 5 mA cm^{-2} is arguably low, lower current cycling was also performed (fig. S17), where average CE% was found to also reach ~99.9%. Additionally, cell cycling at lower stack pressures is also presented in fig. S18. Battery performance described here still represents single-layered pelletized cells with thick SSE separators. The μSi anode's potential for high energy densities (>900 Wh liter^{-1}) can only be realized if SSE thickness can be reduced, in combination

with multilayer form factors (table S5). Nonetheless, the electrochemical results shown above reaffirm the effectiveness of sulfide SSEs in enabling 99.9 wt % μSi anodes, capable of operating with high current densities, over a wide temperature range, and using high areal loadings, as well as achieving a long cycle and calender life. Overall, this approach presents substantial advantages to advance both the silicon anode and ASSB community, offering a pathway to address some of the fundamental interfacial and performance challenges of μSi anodes.

REFERENCES AND NOTES

1. Y. Jin, B. Zhu, Z. Lu, N. Liu, J. Zhu, *Adv. Energy Mater.* **7**, 1700715 (2017).
2. A. Franco Gonzalez, N.-H. Yang, R.-S. Liu, *J. Phys. Chem. C* **121**, 27775–27787 (2017).
3. Y. Yang *et al.*, *Sustain. Energy Fuels* **4**, 1577–1594 (2020).
4. C. Wang *et al.*, *Nat. Chem.* **5**, 1042–1048 (2013).
5. J. Chen *et al.*, *Nat. Energy* **5**, 386–397 (2020).
6. P. Parikh *et al.*, *Chem. Mater.* **31**, 2535–2544 (2019).
7. H. Shobukawa, J. Shin, J. Alvarado, C. S. Rustomji, Y. S. Meng, *J. Mater. Chem. A Mater. Energy Sustain.* **4**, 15117–15125 (2016).
8. H. J. Kwon *et al.*, *Nano Lett.* **20**, 625–635 (2020).
9. Q. Ma *et al.*, *ACS Appl. Energy Mater.* **3**, 268–278 (2019).
10. A. Baasner *et al.*, *J. Electrochem. Soc.* **167**, 020516 (2020).
11. S. Cangaz *et al.*, *Adv. Energy Mater.* **10**, 2001320 (2020).
12. G. Huang *et al.*, *ACS Nano* **14**, 4374–4382 (2020).
13. Y. Wang *et al.*, *Sci. Rep.* **10**, 3208 (2020).
14. W. An *et al.*, *Nat. Commun.* **10**, 1447 (2019).
15. Y. Li *et al.*, *Nat. Energy* **1**, 15029 (2016).
16. S. Choi, T. W. Kwon, A. Coskun, J. W. Choi, *Science* **357**, 279–283 (2017).

17. Z. Xu *et al.*, *Joule* **2**, 950–961 (2018).
18. X. Gao, F. Wang, C. Sam, S. Gollon, C. Yuan, *J. Electrochem. Energy Convers. Storage* **16**, 011009 (2019).
19. J.-G. Ren *et al.*, *Energy Technol. (Weinheim)* **1**, 77–84 (2013).
20. J.-K. Kim *et al.*, *Solid State Ion.* **268**, 256–260 (2014).
21. A. Banerjee, X. Wang, C. Fang, E. A. Wu, Y. S. Meng, *Chem. Rev.* **120**, 6878–6933 (2020).
22. W. Ping *et al.*, *Energy Storage Mater.* **21**, 246–252 (2019).
23. J. Sakabe, N. Ohta, T. Ohnishi, K. Mitsuishi, K. Takada, *Commun. Chem.* **1**, 24 (2018).
24. Y.-G. Lee *et al.*, *Nat. Energy* **5**, 299–308 (2020).
25. R. Xu *et al.*, *ACS Energy Lett.* **4**, 1073–1079 (2019).
26. S. Burkhardt *et al.*, *ACS Energy Lett.* **4**, 2117–2123 (2019).
27. X. Y. Qiu *et al.*, *Phys. Chem. Chem. Phys.* **14**, 2617–2630 (2012).
28. Z. Chen *et al.*, *Adv. Energy Mater.* **5**, 1401826 (2015).
29. D. H. S. Tan *et al.*, *ACS Energy Lett.* **4**, 2418–2427 (2019).
30. T. K. A. Schwietert *et al.*, *Nat. Mater.* **19**, 428–435 (2020).
31. W. Zhang *et al.*, *ACS Appl. Mater. Interfaces* **9**, 35888–35896 (2017).
32. S. Randau *et al.*, *Nat. Energy* **5**, 259–270 (2020).
33. J. Kasemchainan *et al.*, *Nat. Mater.* **18**, 1105–1111 (2019).
34. E. A. Wu *et al.*, *J. Electrochem. Soc.* **167**, 130516 (2020).
35. C. Fang *et al.*, *Nature* **572**, 511–515 (2019).
36. K. Pan, F. Zou, M. Canova, Y. Zhu, J.-H. Kim, *J. Power Sources* **413**, 20–28 (2019).
37. N. Ding *et al.*, *Solid State Ion.* **180**, 222–225 (2009).
38. K. Yoshimura, J. Suzuki, K. Sekine, T. Takamura, *J. Power Sources* **174**, 653–657 (2007).
39. J. M. Doux *et al.*, *Adv. Energy Mater.* **10**, 1903253 (2019).
40. L. A. Berla, S. W. Lee, Y. Cui, W. D. Nix, *J. Power Sources* **273**, 41–51 (2015).
41. V. Kulikovsky *et al.*, *Thin Solid Films* **516**, 5368–5375 (2008).
42. B. Hertzberg, J. Benson, G. Yushin, *Electrochem. Commun.* **13**, 818–821 (2011).
43. F. P. McGrogan *et al.*, *Adv. Energy Mater.* **7**, 1602011 (2017).
44. J.-M. Doux *et al.*, *J. Mater. Chem. A Mater. Energy Sustain.* **8**, 5049–5055 (2020).
45. C. Yu *et al.*, *ACS Appl. Mater. Interfaces* **10**, 33296–33306 (2018).